Exploring the piezoresistive sensing behaviour of ultra-high performance concrete: Strategies for multiphase and multiscale functional additives and influence of electrical percolation

Facheng Song[a, b], Qing Chen[a, *], Mingzhong Zhang[c], Zhengwu Jiang[a], Wenqi Ding[d], Zhiguo Yan[d], Hehua Zhu[d]

[a] Key Laboratory of Advanced Civil Engineering Materials of Ministry of Education, School of Materials Science and Engineering, Tongji University, Shanghai 201804, China

[b] Institute of Advanced Engineering Structures, Zhejiang University, Hangzhou 310058, China

[c] Department of Civil, Environmental and Geomatic Engineering, University College London, London WC1E 6BT, UK

[d] State Key Laboratory for Disaster Reduction in Civil Engineering, Tongji University, Shanghai 200092, China

[*] Corresponding author. E-mail address: 17004@tongji.edu.cn (Q. Chen)

Abstract

Self-sensing ultra-high performance concrete (UHPC) features superior mechanical capacity, excellent erosion resistance, long life cycle, and broad range of stress sensing, and is expected to be a pathway towards next-generation smart cementitious composites. This study presents a novel strategy to achieve electrical percolation and elevate the piezoresistive sensing capability of UHPC through the incorporation of multiphase and multiscale functional additives including graphene (G) and carbon nanotube (CNT). The workability, compressive strength, microstructural characteristics, and alternating current (AC) impedance response are investigated. The effect of electrical percolation on the piezoresistive behaviour is studied and discussed using various ratios of G/CNT. Results indicate that as the G/CNT ratio decreases from 4:0 to 0:4, the compressive strength is reduced from 194.7 MPa to 166.3 MPa due to the certain increase in the plastic viscosity of fresh mixture and the proportion of harmful pores, although the basic requirement of 150 MPa is met. Moreover, the AC impedance response significantly moves left and the radius of high-frequency arc reduces from 72910 Ω to 1295 Ω, suggesting electrical percolation. Bounded by percolation threshold, the fractional change of resistance curves can be divided into a two-stage pattern (i.e., linear and nonlinear stages) and a three-stage mode (i.e., linear decrease, balance, and abrupt increase stages). An underlying mechanism is proposed to explain the tremendous change in piezoresistive behaviour of self-sensing UHPC, considering the tunnelling-percolation theory and electromechanical coupling behaviour. Additionally, the gauge factors range from 11 to 28, which is higher than most of the existing reported values, demonstrating the great potential of using hybrid functional nano-additives in self-sensing UHPC.

Keywords

Self-sensing ultra-high performance concrete; Graphene; Carbon nanotube; Electrical percolation; Piezoresistivity

1 Introduction

Structural health monitoring (SHM) is of tremendous significance to construction and maintenance of civil infrastructure [1]. One of the main steps in setting up an effective SHM system, in general, is the selection of stable and credible sensing tools or sensors [2]. Self-sensing cementitious composites can sense the structures' healthy conditions without the external sensors, which provide advantages of easily coupling with the monitored concrete structures, long life span, and reasonable cost compared with the conventional commercial sensors [3, 4]. They are fabricated by incorporating different types of functional additives, such as electrically conductive sheets (e.g., graphene (G), reduced graphene oxide, and exfoliated graphite), fibres (e.g., carbon fibre, steel fibre, and carbon nanotube (CNT)), and powder (e.g., metal powder, carbon black, and steel slag), in dielectric cement-based matrices (e.g., cement paste, mortar, and concrete) [5-10].

Today, because of superior mechanical properties and durability, ultra-high performance concrete (UHPC) has been widely adopted in various infrastructure constructions such as buildings, bridges, and military structures [11-14]. When applied to the UHPC elements, self-sensing ordinary cementitious composites (OCC) can lose the benefit of excellent compatibility with the monitored structures and easily become the weakest part of the section [15]. Specifically tailoring UHPC with self-sensing properties is an efficient engineering solution to meet the SHM requirements of the aforementioned robust and durable civil infrastructures. Note that the effect of the transition of matrix type (i.e., from OCC to UHPC) on self-sensing capability and behaviour remains unclear, it is therefore difficult to apply and extend the previous results to UHPC directly. Some focuses have been placed on piezoresistive and self-sensing behaviour of UHPC [16]. For instance, several attempts have been made to exploit the inherent self-sensing potential of UHPC by tailoring fibres [15, 17-19] and aligned fibre distribution [20]. The fibres used are reported competent for the construction of an effective conductive network and for improving the inherent self-sensing capability of UHPC. Further, given the superior mechanical and electrical properties, carbon nanomaterials such as CNT [21-24] and G [25, 26] were employed to improve the self-sensing capacity of UHPC. It was found that the electrical resistivity of UHPC can be significantly reduced by using carbon nanomaterials, which can generate contact with the surface of steel fibres and steel fibre plays more important roles in the mechanical properties than electrical behaviour [22, 26]. To enhance the contacting conduction and self-sensing ability, steel slag aggregates [27], metal powders [28], nanocarbon black [29], and carbon nanofiber [30] were also incorporated into UHPC matrix.

Overall, the existing studies are mainly focused on the mixtures containing steel fibre [15, 17-20], conductive aggregates [27], and single carbon nanomaterials [21-26, 28-30]. Although they have demonstrated the viability of achieving self-sensing in a UHPC mixture, the research on self-sensing UHPC is still in its infancy and faces some big challenges. It was reported that self-sensing UHPC exhibits considerably linear compressive stress-strain behaviour up to the peak stress while the fractional change of resistance (FCR) value is indistinguishable until 70% of the ultimate strain [21], indicating the current low-level strain sensitivity of self-sensing UHPC. The connectivity of conductive network (i.e., electrical conductivity) can be improved by increasing the number of functional fillers incorporated, which is considered as an efficient way to enhance the sensitivity of self-sensing cementitious materials [9], but it also leads to low workability, high viscosity, and agglomeration of functional additives, especially for UHPC [12, 31]. The properties like electrical conductivity of multi-phase materials are highly dependent on the volume fraction, size, and distribution of additives in the composites [32]. Thus, regarding the design and manufacture of self-sensing cementitious composites, the addition of different multiscale conductive fillers has become a common method because of the possible synergistic effect on reducing the number of fillers necessary to achieve electrical percolation and elevating the sensing capability [22, 32, 33]. The equivalent sensing capability can be achieved as a mono-filler using less total amount of conductive fillers [22]. There exists an excellent synergetic effect between 1D CNT and 2D G on physical and chemical properties of cementitious composites [33], indicating the immense potential of employing hybrid of them to develop self-sensing UHPC. However, to the best knowledge of the authors, the coupling effect of CNT and G on piezoresistive and self-sensing behaviour of UHPC, considering the effect of electrical percolation on piezoresistive behaviour, has been rarely explored.

The main purpose of this study is to systematically investigate the piezoresistive behaviour of self-sensing UHPC with hybrid G and CNT through a series of tests including mechanical test, alternating current impedance spectroscopy (ACIS) test, and piezoresistive test, focusing on the effect of electrical percolation. Given the low water-to-binder (w/b) ratio, the workability that can affect the electromechanical properties was also characterized, as well as the dispersion of carbon nanomaterials, pore structure, morphology, and interfacial transition zone (ITZ) in self-sensing UHPC matrix, which were characterized and evaluated using mercury intrusion porosimetry (MIP) and scanning electron microscope-energy dispersive spectrometer (SEM-EDS). Based on the microscopic and macroscopic observations, the underlying mechanisms of piezoresistive behaviour of self-sensing UHPC were discussed in depth. The findings advance the understanding of the piezoresistive sensing behaviour of percolated UHPC and lay the foundation for the engineering application of self-sensing UHPC with multiphase and multiscale functional additives.

2 Materials and methods

2.1 Materials

Portland cement Type II 52.5 N and 970U silica fume were chosen as binders for UHPC, the specific surface area of which is 0.367 and 21 m^2/g, respectively. The chemical compositions of Portland cement and silica fume as determined by X-ray fluorescence spectrometer (XRF) are given in Table 1. Quartz powder with a particle size of 8000 mesh was adopted as inactive filling material, and quartz sand with a mean diameter ranging from 0.15 to 0.6 mm was used as aggregate. Polycarboxylate-based superplasticizer (SP) with a 21% water-reducing rate was added to improve the dispersing efficiency of carbon nanomaterials in water for all mixtures and the workability of fresh mortar. Straight steel fibre plated with golden-colour copper was used, whose fundamental properties are enumerated in Table 2. Table 3 lists the specific gravity of these raw materials.

Table 1 Chemical compositions (wt.%) of Portland cement and silica fume.

Typical oxide	CaO	SiO_2	Al_2O_3	Fe_2O_3	SO_3	K_2O	MgO	Na_2O	LOI
Portland cement	63.63	20.86	4.47	3.12	2.51	0.71	1.45	0.30	2.57
Silica fume	0.52	96.20	0.26	0.06	0.54	0.31	0.57	0.21	1.25

Table 2 Properties of copper-plated straight steel fibre.

Length (mm)	Aspect ratio	Density (g/cm^3)	Tensile strength (MPa)	Elastic modulus (GPa)
13	65	7.85	2850	200

Table 3 Specific gravity of different ingredients (expect fibre) in composites.

	Portland cement	Silica fume	Quartz powder	Quartz sand	SP
Specific gravity	3.05	2.10	2.63	2.63	1.12

Carbon nanomaterials including G and CNT were used to improve inherent self-sensing capability of UHPC, the physical properties of which are presented in Tables 4 and 5, respectively. These properties are provided by the manufacturer. The microscopic images of them are demonstrated in Fig. 1. As seen in Fig. 1a, the pulverous G agglomerates present lamellar shapes and rough surfaces. After the treatment of alcohol dissolution and ultrasonic dispersion, G practically shows a thin thickness and large specific surface area. Fig. 1b indicates that the nanoscale CNTs are intricately entangled into clusters. It is crucial to ensure that the carbon nanomaterials used in this study are adequately dispersed in suspensions before being added to UHPC matrix.

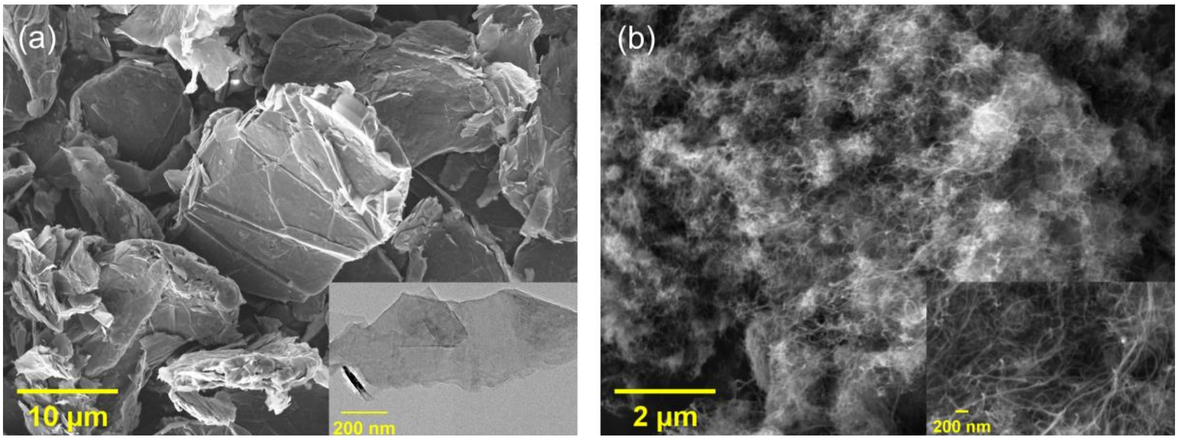

Fig. 1. SEM image of (a) G with insert showing the high-resolution TEM image and (b) CNT with insert highlighting the high-magnification SEM image.

Table 4 Properties of graphene (G).

Layers	Lateral size (μm)	Thickness (nm)	Purity (%)	Density (g/cm^3)	Content of C (%)	Content of O (%)	Specific surface area (m^2/g)
5-10	5-50	3.4-8	95	2.23	>98	<2	50

Table 5 Properties of carbon nanotube (CNT).

Inter mean diameter (nm)	Outer mean diameter (nm)	Length (μm)	Purity (%)	Density (g/cm^3)	Specific surface area (m^2/g)
3-5	8-15	3-12	>91	2.10	>233

2.2 Mix proportions

Table 6 presents the mix proportions of UHPC with G and CNT (G/C-UHPC) studied here. A constant w/b ratio of 0.24 and a volume fraction of 2% of steel fibre were adopted. It was reported that the electrical percolation threshold of CNT in cementitious composites ranged from 0.5% to 0.6% (by weight) of the incorporated cement [34] and the threshold for electrical conductivity of 2D G is higher than 1D CNT in composite materials [10]. To investigate the piezoresistive behaviour of self-sensing G/C-UHPC before and after electrical percolation, the hybrid mass of carbon nanomaterials was fixed as 0.5% of binders and five G/CNT ratios, including 4:0 (G4C0), 3:1 (G3C1), 2:2 (G2C2), 1:3 (G1C3), and 0:4 (G0C4), were considered. Since CNT has a smaller density than G, the total volume and specific surface area of carbon nanomaterials in UHPC matrix gradually go up with the CNT dosage. The content of SP varied with the ratio of carbon nanomaterials to satisfy the workability requirements of fresh mixture and the dispersion needs of carbon nanomaterials [26].

Table 6 Mix proportions of G/C-UHPC (kg/m^3).

ID	Portland cement	Silica fume	Quartz powder	Quartz sand	Water	Steel fibre (vol. %)	SP	G	CNT
G4C0	726	87	244	1045	195	2	7.87	4.0650	0
G3C1	726	87	244	1045	195	2	10.16	3.0488	1.0163
G2C2	726	87	244	1045	195	2	12.20	2.0325	2.0325
G1C3	726	87	244	1045	195	2	14.23	1.0163	3.0488
G0C4	726	87	244	1045	195	2	16.26	0	4.0650

2.3 Dispersion of carbon nanomaterials and specimen preparation

Uniformly distributed carbon nanomaterials in concrete are critical to the enhancement of its physical and chemical properties [5]. Ultrasonication combined with surfactants was the effective approach to ensure the well-dispersion of carbon nanomaterials, as demonstrated in previous studies [5]. Thus, similar dispersion steps were employed here: (1) The G, CNT, and SP in each group were mixed with three quarters of the water in a glass beaker and the mixture was stirred by a glass rod until there was no visible powder on the surface of suspension. (2) An ultrasonic cleaner (40 kHz, 540 W) was used for the ultrasonic process with a duration of 15 min. It is noteworthy that excessive total ultrasonic energy can destroy the intrinsic structures of carbon nanomaterials [35] and it is difficult to balance the tradeoff between the dispersion degree and the resulting damage. In view of the inevitable temperature rise induced by continuous ultrasonic, the beakers containing suspension were rinsed under running water to cool down to an ambient temperature (25 °C). The prepared suspensions were left to stand for standby applications.

All G/C-UHPCs were fabricated by identical mixing procedure via a Hobart-type cement mortar mixer to reduce the discreteness of experimental results. Cement, silica fume, quartz powder, and quartz sand were first premixed to ensure homogeneous dispersion of dry solid components. Second, the prepared suspensions and remaining quarter of mixing water were poured into the dry mixture and stirred at fast speed (285 ± 10 r/min) for 5-8 min until the fresh concrete presented a fluid state. Third, steel fibre was gradually added at low speed (140 ± 5 r/min), followed by fast-speed stirring until uniformly dispersed in the mixture. Afterwards, the final mixtures were disposably cast into the pre-oiled moulds (the cubic moulds of 70.7 mm × 70.7 mm × 70.7 mm for mechanical test and the dimension of 40 mm × 40 mm × 160 mm for piezoresistive behaviour and ACIS measurement). Meanwhile, four stainless steel plates with round holes (ϕ5) were inserted as electrodes into the specified position of the specimens, as illustrated in Fig. 2. The reason for choosing this form of electrode is to minimize the influence of the electrode insertion on the distribution of steel fibres in UHPC mixtures [26]. All specimens were covered with plastic sheets, placed at room temperature, and then demoulded after 24 h, following by curing in a steam curing box at 90 °C for 48 h and drying in a thermotank at 105 °C for 48 h prior to test to remove free moisture from the specimen.

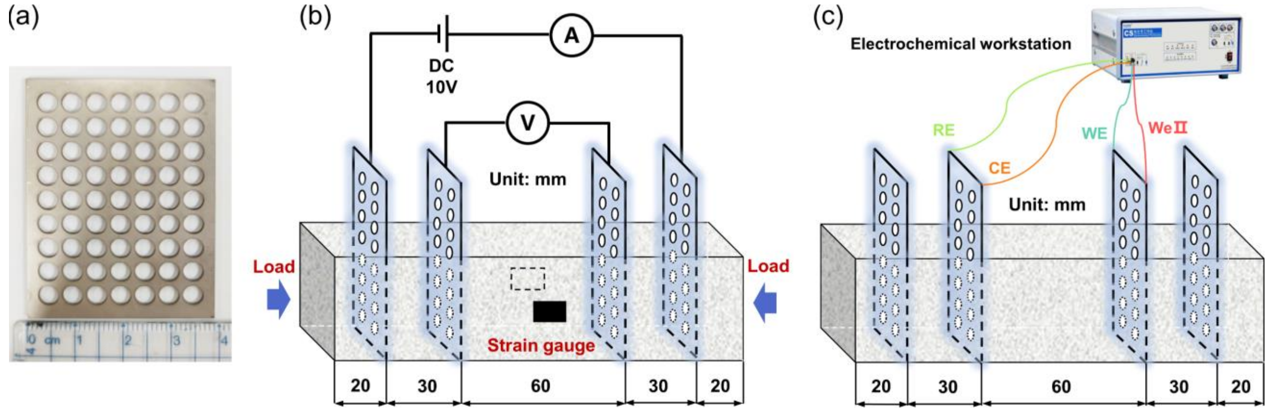

Fig. 2. (a) Photo of the stainless-steel plate with circular holes, schematic diagrams of (b) the piezoresistive test and (c) the ACIS measurement. Note: RE = reference electrode, WE = work sense electrode, CE = counter electrode, and WeII = work force electrode.

2.4 Test methods

2.4.1 Rheological test

The rheological parameters of cement pastes were measured using DVNext rotational rheometer with SC4-27 rotor and SC4-13RP specimen cup. The following test sequence was adopted: (1) Binders, carbon nanomaterials, and mixing water were mixed by the cement paste mixer as per ASTM C305-2. (2) Approximately 10 mL of paste was placed in the specimen cup. (3) The test procedures (Fig. 3) comprising pre-shearing, rest, and data acquisition processes were employed. Three concurrent tests were performed and the mean value for each group was taken.

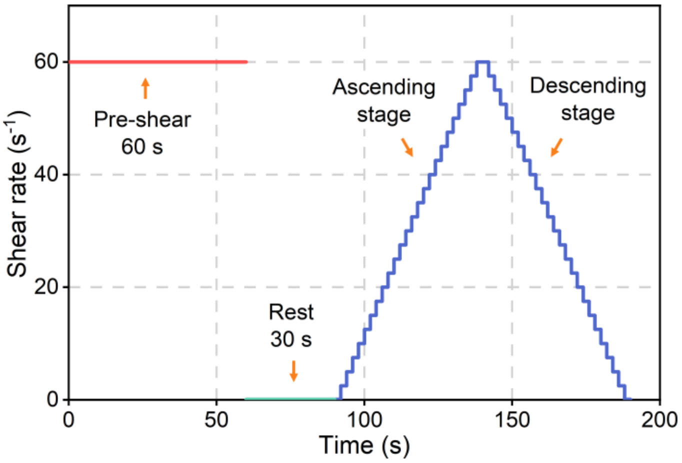

Fig. 3. Representation of rheological test procedure.

2.4.2 Mechanical test

The compressive strength and elastic modulus of specimens were measured using a 3000 kN test machine with a loading rate of 1.5 kN/s in accordance with ASTM C109/C109M-13. The compressive strain parallel to the load was determined by vertically putting up two strain gauges on the opposite sides of specimen. The strain values were recorded by the statical strain acquisition instrument TST3822 and the averaged values were used. Additionally, the modulus of elasticity was obtained from the partial compressive stress *vs* strain curve according to ASTM C469/C469M-14 and the average of three non-interfering test results was taken.

2.4.3 Scanning electron microscopy and energy dispersive spectrometry

The morphology of crushed specimens and microstructure of hardened G/C-UHPC were characterized using scanning electron microscopy-energy dispersive spectrometry (SEM-EDS, Sigma 300 VP) at 10 kV [36, 37]. The specimens were cut into pieces (10 mm × 15 mm × 15 mm). The isopropanol solvent exchange method was adopted to stop the hydration in the specimens. After vacuum drying at 40 °C, the prepared specimens were impregnated in epoxy resin. Afterwards, the grinding and polishing processes were conducted using silicon carbide grinding papers (grit sizes of 600, 800, 1200, 1500, 2500, and 4000 sequentially) and two types of ultra-fine diamond suspensions

(3 μm and 0.25 μm), respectively. Ultrasonic bath cleaning was used to rinse all dust and diamond particles off. The specimens were gilded and carbon-coated prior to microscope imaging.

2.4.4 Mercury intrusion porosimetry

Mercury intrusion porosimetry (MIP, AutoPore IV 9500) was employed to characterize the pore structure of G/C-UHPC. Before the test, specimens were cut into 5 mm × 5 mm × 5 mm pieces and dried in a vacuum oven at 40 ℃ for 48 h. The tested pore diameters ranged from 5 nm to 500 μm.

2.4.5 Alternating current impedance spectroscopy test

As illustrated in Fig. 2c, the ACIS measurement was carried out on CS350H electrochemical workstation to measure the electrical properties of G/C-UHPC following the two-electrode method, which is one of the most common approaches [20, 27]. The work sense electrode (WE) and work force electrode (WeII) connected with one of the inner stainless-steel plates while the counter electrode (CE) and reference electrode (RE) led to the other. The applied alternating current voltage amplitude was 20 mV, and the test frequency ranged from 0.01 Hz to 1 MHz, following with the existing report [26]. Six specimens for each group were measured and the mean value was obtained for analysis.

2.4.6 Piezoresistive test

Regarding the use of direct current (DC) or AC in piezoresistive test, in general, DC resistance has received more attention than the AC impedance in relation to piezoresistivity. As argued by Chung [3, 9, 38], scanning the impedance over a wide range of frequency needs time and is not appropriate for real-time monitoring, although the AC method is advantageous for the lower degree of electric polarization. The DC method is simpler and has greater degree of current penetration. Therefore, the piezoresistive properties of G/C-UHPC were evaluated using the four-point method here, with the inner two electrodes measuring voltage and the outer two measuring current. As shown in Fig. 2b, the electrical resistance at any moment (R_t) was measured by an isobaric DC power source with applied value of 10 V and calculated by Ohm's law in terms of currents (I_t) and voltages (U_t) obtained from two date acquisition units:

$$R_t = U_t/I_t \tag{1}$$

The compressive strain perpendicular to the electrodes was determined by attaching two strain gauges to the opposite sides of the middle of specimen. Two FR-4 fibreglass plates with a size of 100 mm × 100 mm × 5 mm were placed between the test clamp and specimen to prevent extra current flow. Considering the polarization effect that occurs when using DC, all specimens were subjected to a one-hour charged wait process prior to the piezoresistive test [26]. Although the relaxation polarization inside G/C-UHPC tends to take longer to reach the polarization equilibrium [26], the current fluctuation can be reduced to a satisfactory level here. Two kinds of compressive loads (Fig. 4) consisting of monotonic (loading rate of 1.5 kN/s) and cyclic load (maximum stress values of 40, 60, and 80 MPa in different cycles) were applied to the piezoresistive specimen after the variations in voltage and current became stable. The load, strain, voltage, and current values were recorded throughout the loading process. Three specimens were tested for each group and the mean value was gained. The FCR and gauge factor (GF) can be expressed as [9]:

$$FCR = (R_t - R_0)/R_0 \times 100\% \tag{2}$$

$$GF = |FCR/\varepsilon| \tag{3}$$

where R_0 signifies the initial electrical resistance.

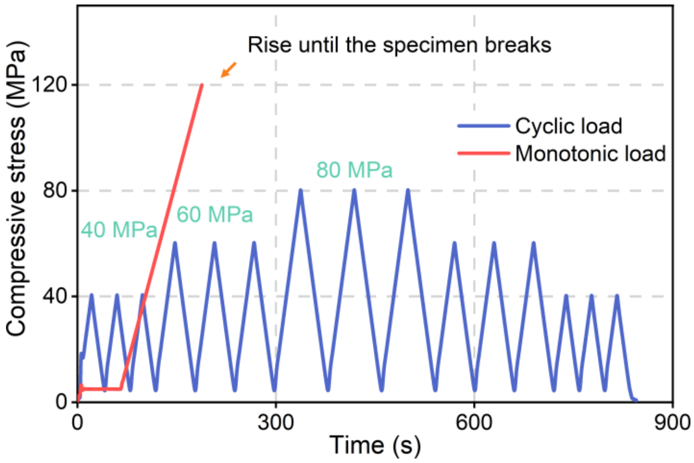

Fig. 4. Loading methods for the piezoresistive test.

3 Results

3.1 Workability

The evaluation of rheological behaviour of cementitious suspensions can provide valuable information on the workability of fresh concrete, especially for UHPC [39]. Fig. 5 illustrates the flow curve (shear stress *vs* shear rate) of all specimens plotted as per the descending stage of the shearing process. No sedimentation or segregation was observed throughout the shearing test. It is indicated that the shear stress gradually increased with the decline of G/CNT ratio. The rheological characteristics of fresh concrete can be estimated using parameters including yield stress (τ_0) and plastic viscosity (η_p) [40]. The Bingham model can be, in general, used to well describe these two rheological parameters for cement-based materials as [40]:

$$\tau = \tau_0 + \eta_p \dot{\gamma} \tag{4}$$

where τ and $\dot{\gamma}$ are the shear stress and shear rate, respectively.

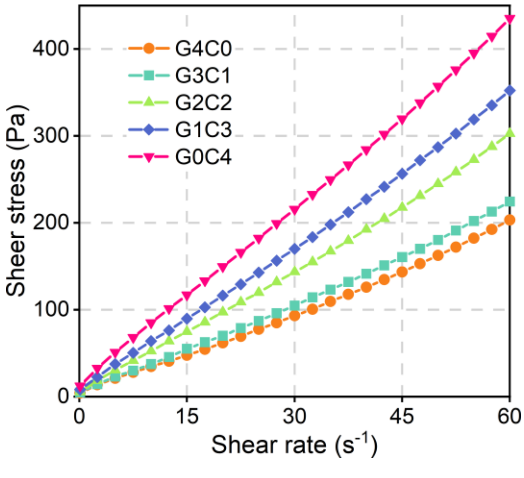

Fig. 5. Flow curve of cement paste with various G/CNT ratios.

Table 7 lists the fitting results of the data presented in Fig. 5 using Eq. (4). Noting that the yield stress of G4C0 was -0.129, implying that the Bingham model may not be applicable to the mixtures studied, as the appearance of negative yield stress is physically impossible. This is consistent with the previous finding that the traditional Bingham model cannot accurately describe the low shear stress obtained in the lower and unstable shear rate region of the flow curve [40]. To avoid negative values and better extrapolate the yield stress and plastic viscosity, the modified Bingham model, i.e., Eq. (5), was used instead [40]:

$$\tau = \tau_0 + \eta_p \dot{\gamma} + c\dot{\gamma}^2 \tag{5}$$

where c denotes the second-order parameter (Pa·s^2).

The approximate results are listed in Table 7 also, indicating a perfect fitting with R^2 of close to one. As observed, the decrease in G/CNT ratio led to a rise in yield stress and plastic viscosity. The yield stress and plastic viscosity relative to G4C0 went up by -4.2%, 21.2%, 55.4%, 148.6% and 18.7%, 67.2%, 101.0%, 155.6%, respectively, with the decline of G/CNT ratio from 3:1 to 0:4. This trend can be ascribed to the rise of specific surface area of nanomaterials, which makes cement paste require additional water for lubrication due to the nanomaterials' multilayer structure (high specific surface area) and reduces the content of water in unit volume of paste [41]. In addition, during the shearing process, floccules can generate between nanomaterials and cementitious particles through electrostatic interaction, rising the friction forces and surface contacts between particulates with the change of nanomaterials, which further increases the rheological parameters [40].

Table 7 Rheological parameters and fitting results by different rheological models.

ID	Bingham model			Modified Bingham model			
	η_P	τ_0	R^2	η_P	τ_0	c	R^2
G4C0	3.241	-0.129	0.99559	2.462	7.354	0.013	0.99972
G3C1	3.596	0.584	0.99732	2.923	7.042	0.011	0.99982
G2C2	4.856	1.820	0.99812	4.117	8.910	0.012	0.99978
G1C3	5.643	4.770	0.99876	4.949	11.427	0.012	0.99984
G0C4	6.893	12.540	0.99917	6.294	18.280	0.010	0.99971

3.2 Compressive strength and elastic modulus

In Fig. 6a, the mean compressive stress-strain curves of G/C-UHPC are plotted, which were obtained by averaging three independent data points based on the strain of each mixture and ignoring the error bands. Most of the curves show analogous two-stage topological structure including the linear-elastic and nonlinear stages, which agrees well with the previous study [42] that UHPC demonstrates a linear limit up to 70%-95% of the amplitude of compressive stress. This suggests that the macroscopic deformation and cracking processes under uniaxial compression tend to be similar for different specimens, despite the diverse values of the peak stress.

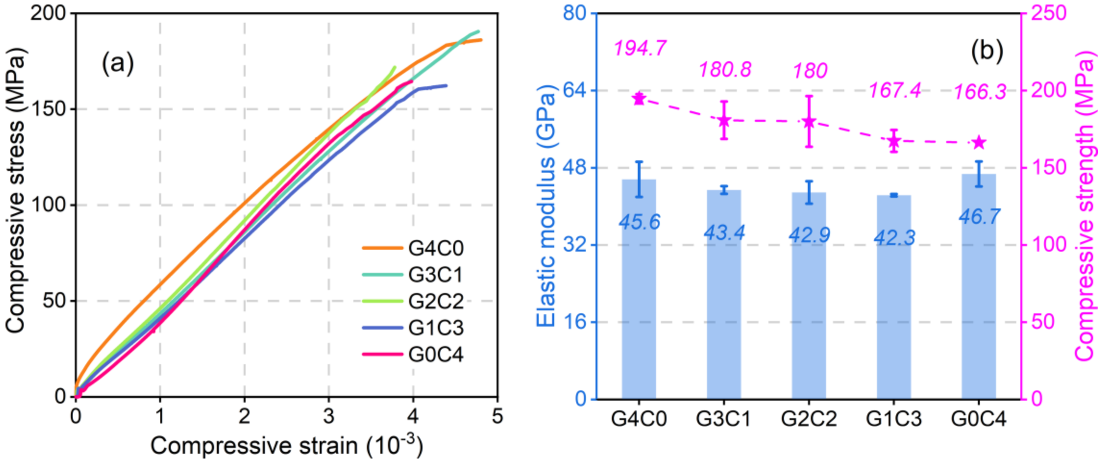

Fig. 6. (a) Compressive stress-strain curve, which is obtained by averaging three independent data points based on the strain of each mixture and ignoring the error bands, (b) elastic modulus and compressive strength of G/C-UHPC with various G/CNT ratios.

Fig. 6b summarizes the compressive strength and elastic modulus of G/C-UHPC. As the ratio of G/CNT decreased, a general downtrend can be observed for the compressive strength of G/C-UHPC with fixed steel fibre content, although it satisfied the basic requirement of 150 MPa [43]. Specifically, compared to G4C0, the compressive strength dropped by 7.1%, 7.6%, 14.0%, and 14.6%, respectively. The strength reduction can be associated with the formation of weak zones inside G/C-UHPC, resulting from the diminution of workability reflected by the increment of rheological parameters. Results here are inconsistent with the finding reported in Ref. [44] that the hybrid graphene materials and carbon nanotube exhibited a synergistic effect on the compressive strength of cement paste when the total dosage of carbon nanomaterials was kept consistent. The discrepancy can be mainly attributed to the higher dosage of nanomaterials (i.e., 0.05% of cement adopted in Ref. [44]) and more compact matrix in this study, where the weak zones might more considerably reduce the compressive strength compared to OCC [24]. The hybrid ratio of carbon nanomaterials did not signally impact the elastic modulus of G/C-UHPC, which is due to the low content of carbon nanomaterials [45-47].

3.3 Microstructural characteristics

3.3.1 Micromorphology observation

Fig. 7 depicts a representative backscattered electron (BSE) diagram and EDS area analysis for specimen G4C0. The distribution of carbon nanomaterials in UHPC matrix was comprehensively identified by taking the EDS results, specific morphology contrast, and atomic number contrast into consideration [48]. As indicated by the yellow arrows, the dark region with a slender and curving morphology in Fig. 7a was simultaneously highlighted in the carbon element distribution of the selected area (Fig. 7b), which can be therefore speculated as G. It can be observed that G flakes were uniformly distributed in G4C0, indicating that G was well dispersed in UHPC matrix.

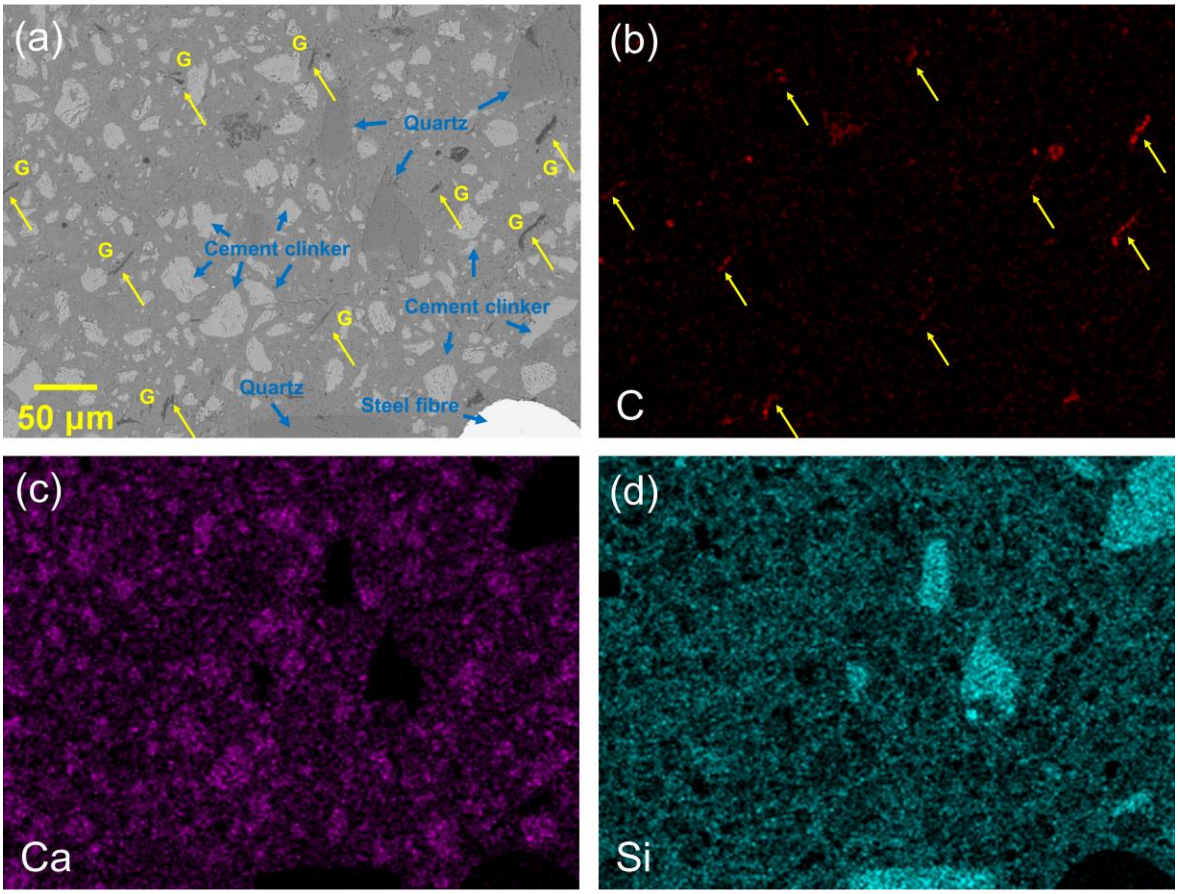

Fig. 7. (a) Typical BSE image of specimen G4C0 and (b-c) the corresponding elemental maps for C (red), Ca (purple), and Si (cyan).

As seen in Fig. 8a, G (spot A), quartz (spot B), hydration products (spot C), and cement clinker (spot D) can be recognized by roundly using the atomic number contrast and EDS results. G provided abundant adhesion sites for hydration products and formed strong bonds with them [26]. A similar result is illustrated in Fig. 8b, where the lamellar G was tightly anchored in the hardened matrix, and it is difficult to detect the debonding of the G-matrix interface in the specimen even after crushing. From Fig. 8e, the high-aspect-ratio CNTs were encapsulated by hydration products and a few CNTs were pulled out between the cracks. CNT was embedded at both sides of the cracks and presented a crack-bridging effect [49]. As shown in Fig. 8c and d, CNT formed bridges between adjacent G lamella, thereby establishing a filler distribution network that improved the external stress-bearing capacity. Nonetheless, as CNT proportion increased, a few clumped CNT bundles can be observed in UHPC matrix (Fig. 8f).

As a fibre reinforced concrete, the mechanical properties of G/C-UHPC are closely related to the fibre-matrix bonding performance mainly dominated by the strength of fibre, surrounding hydration productions, and interfacial transition zones (ITZs) [11]. Fig. 9 displays the morphological features of steel fibres and their vicinity in different specimens. Steel fibres in G4C0 (Fig. 9a and b) and G2C2 (Fig. 9c and d) were firmly bound to the hardened matrix, and the interfacial weakness zone or fibre-matrix debonding cannot be discovered. For G0C4 (Fig. 9e and f), there were several cracks derived from the fibre and debonding of the fibre-matrix interface on the observation surface. This can be explained by the fact that the promoted water absorption capacity of carbon nanomaterials improved the cohesion of the cementitious composites and weakened the bond between the matrix and fibre [11].

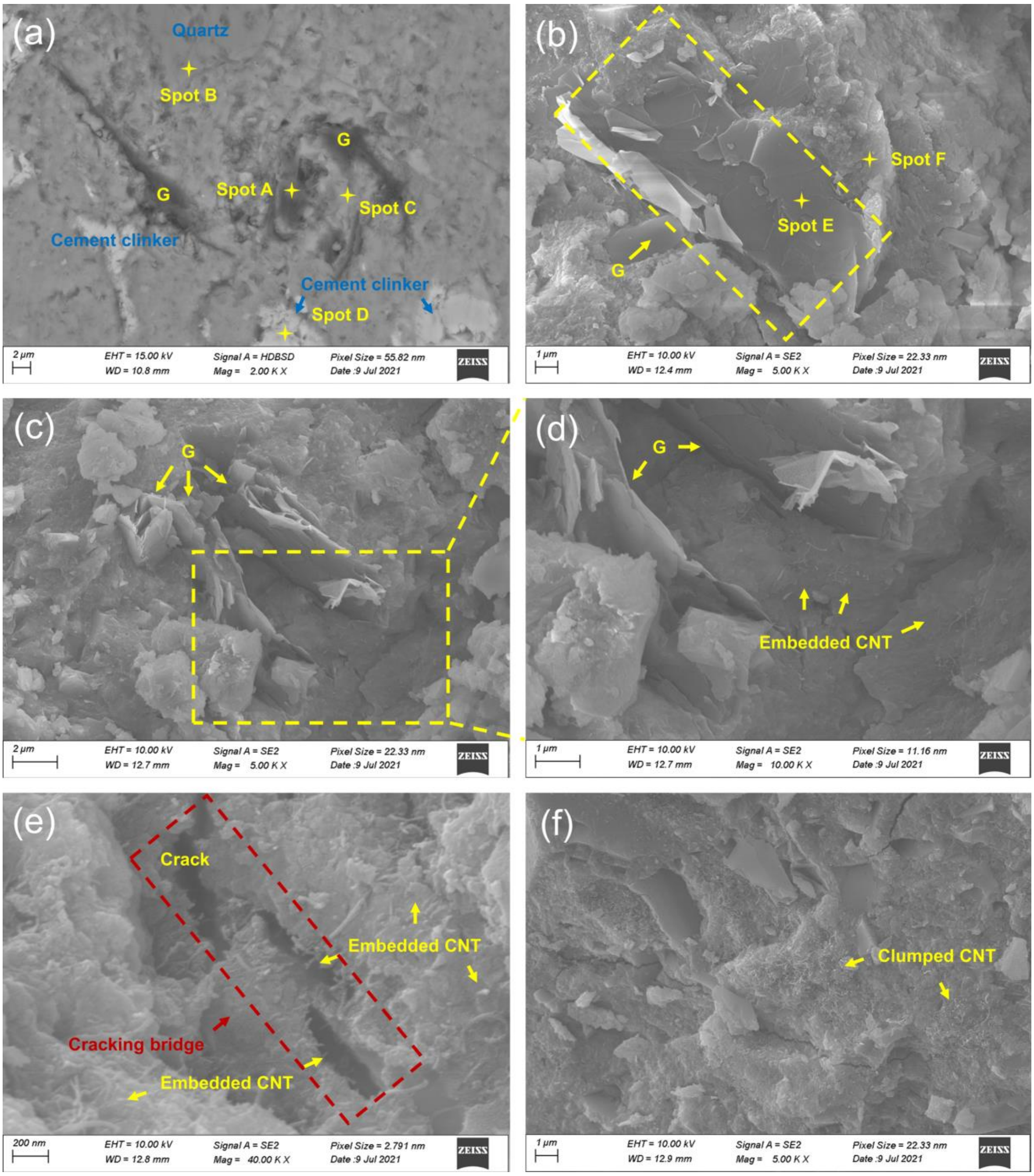

Fig. 8. SEM images for G/C-UHPC: (a) & (b) G4C0, (c) & (d) G2C2, and (e) & (f) G0C4.

Table 8 Chemical compositions from EDS analysis of selected spots in Fig. 8 (Atomic %).

Spot	A	B	C	D	E	F
C Kα1	81.34	18.92	31.42	23.69	75.71	18.59
O Kα1	9.71	58.33	44.16	44.45	12.23	58.17
Ca Kα1	3.93	2.39	8.49	23.21	3.85	9.37
Si Kα1	4.41	20.10	14.57	7.92	5.51	9.62

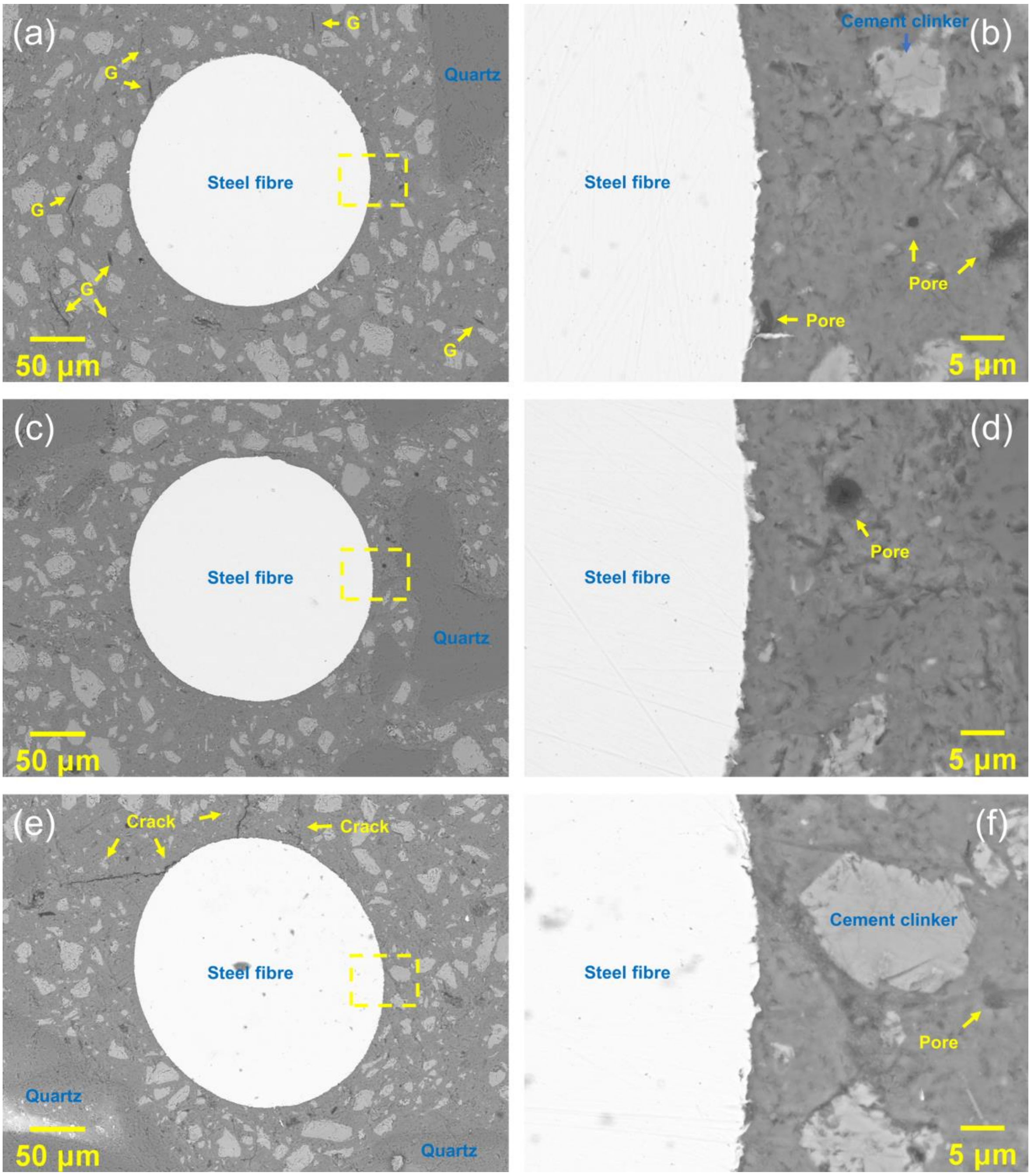

Fig. 9. Morphological features of embedded steel fibres and their vicinity in G/C-UHPC: (a) & (b) G4C0, (c) & (d) G2C2, and (e) & (f) G0C4.

3.3.2 Pore structure

In general, the classification of the pores in concrete science contains different levels from micro to meso to macro, which can be categorized into four regions, including Region I (air holes, >100000 nm), Region II (large capillary pores, 50-100000 nm), Region III (medium capillary pores, 10-50 nm), and Region IV (gel pores or small capillary pores, 2-10 nm) [50]. Among them, pores with size more than 50 nm are customarily deemed to be harmful pores [50].

Fig. 10 demonstrates the MIP results for G/C-UHPC. As seen in Fig. 10a, the pore size distribution (PSD) of specimens was significantly affected by the mass ratio of the incorporated carbon nanomaterials. The peak heights in region IV reduced, which can be attributed to the step-down hydration degree triggered by its enhanced water absorption capacity [51]. As the proportion of CNT increased, the peak numbers in region III decreased and the PSD curves shifted inward, indicating pore refinement due to the inactive filling effect of CNT [52]. For G0C4, as the volume of small and medium capillary pores declined, the total volume of large capillary pores and air holes (i.e., harmful pores) increased. Fig. 10b gives the cumulative PSD curves for G/C-UHPC. The curves shifted downward as the mass ratio of G/CNT dropped, implying the pore refinement. The porosity first diminished and then increased as G/CNT ratio decreased (Fig. 10c). Compared to G4C0, the total porosity of G3C1, G2C2, G1C3, and G0C4 decreased by 25.1%, 35.0%, 42.8%, and 26.8%, respectively.

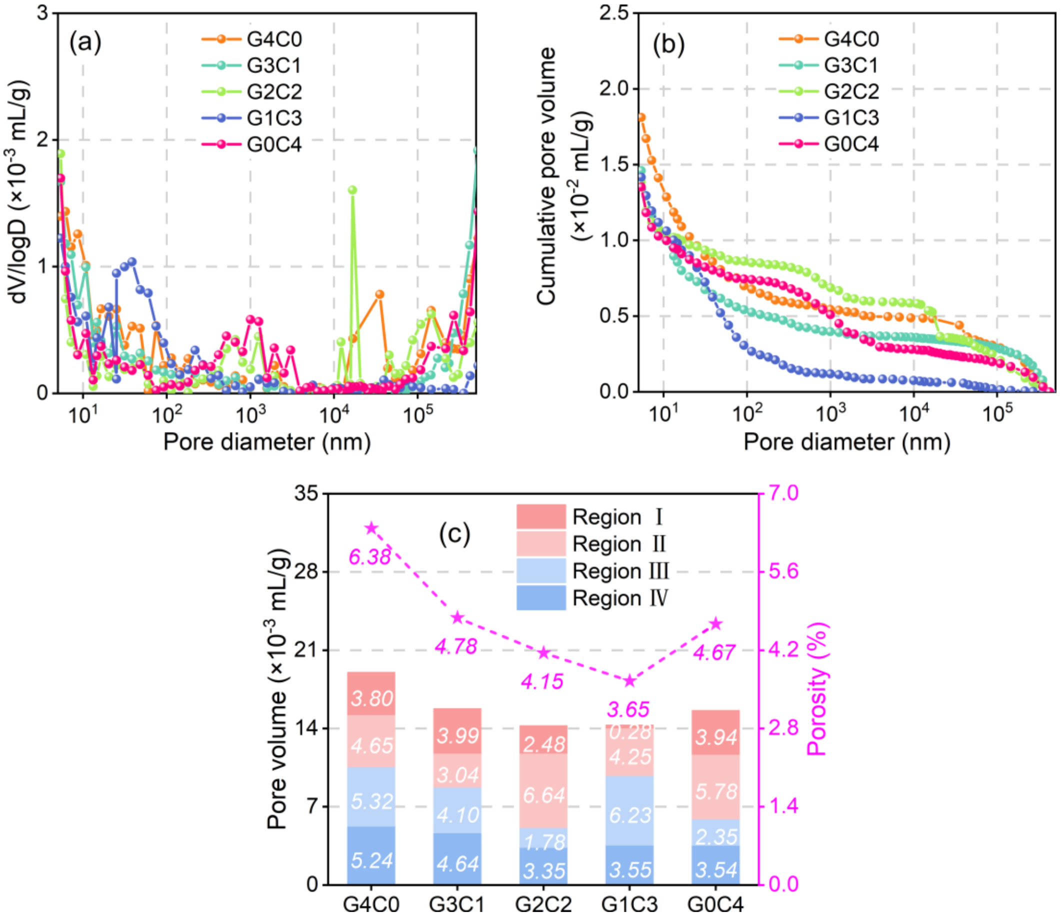

Fig. 10. PSD and porosity for G/C-UHPC obtained from MIP.

3.4 Alternating current impedance response

The normalized ACIS results for actual electrode spacing of G/C-UHPC are presented in the form of complex plane impedance plot in Fig. 11. Eighty points were collected over the entire frequency range, all of which were plotted with decreasing frequency from left to right. The impedance response shifted to the left and the impedance value decreased by several orders of magnitude as the ratio of G/CNT declined. The topological structure of the Nyquist plot was completely altered as follows: (1) G4C0: a straight line on the low-frequency side and a circular arc at the high-frequency region. (2) G3C1 and G2C2: an additional U-shaped valley and a circular arc at the intermediate-frequency region compared with G4C0, respectively. (3) G1C3: a straight line with positive slope on the low-frequency side, a circular arc at the intermediate-frequency region, and another circular arc at the high-frequency region. (4) G0C4: a circular arc on the low-frequency side and another circular arc at the high-frequency region.

In order to obtain quantitative information on the volumetric electrical response of G/C-UHPC [53], the circular and linear fits were performed on the representative data points at the high- and low- frequency regions of the Nyquist diagram. The fitting results indicate that as G/CNT ratio decreased from 4:0 to 0:4, the radius value gradually decreased from 72910 Ω to 1295 Ω along with a pronounced decline in G1C3 and G0C4, implying the occurrence of electrical percolation [21, 34]. For the arcs on the low-frequency side, G0C4 and G1C3 presented, respectively, an arc intersecting the horizontal axis of Nyquist plot and a straight line with a positive slope, while the remaining specimens showed a straight line with a negative slope. In view of the aforementioned results, these morphological structures are closely related to the integrity of conductive network inside specimen. Before electrical percolation, that is, for G4C0, G3C1, and G2C2, a continuous conductive network has not been established throughout UHFRC matrix, and the imaginary part of impedance went to infinity at low frequencies as a constant current cannot flow through the system. In contrast, the impedance became real at $\omega \rightarrow 0$ indicates that a DC may circulate in G1C3 and G0C4. This can be attributed to that the content of carbon nanomaterials in the unit volume of cementitious composites increased with the mass proportion of CNT, which not only improved contacting conduction, but raised the possibility of tunnelling conduction [54].

Fig. 12 displays the frequency-dependent volumetric conductivity of G/C-UHPC obtained from impedance responses [53]. With frequency across the entire test range, the volumetric conductivity of all specimens went up one to three orders of magnitude and the underlying cause was dielectric polarization [53]. At frequencies less than 1 kHz, the volumetric conductivity of G1C3 and G0C4 was elevated by one to two orders of magnitude in contrast to that of G0C4, also indicating electrical percolation.

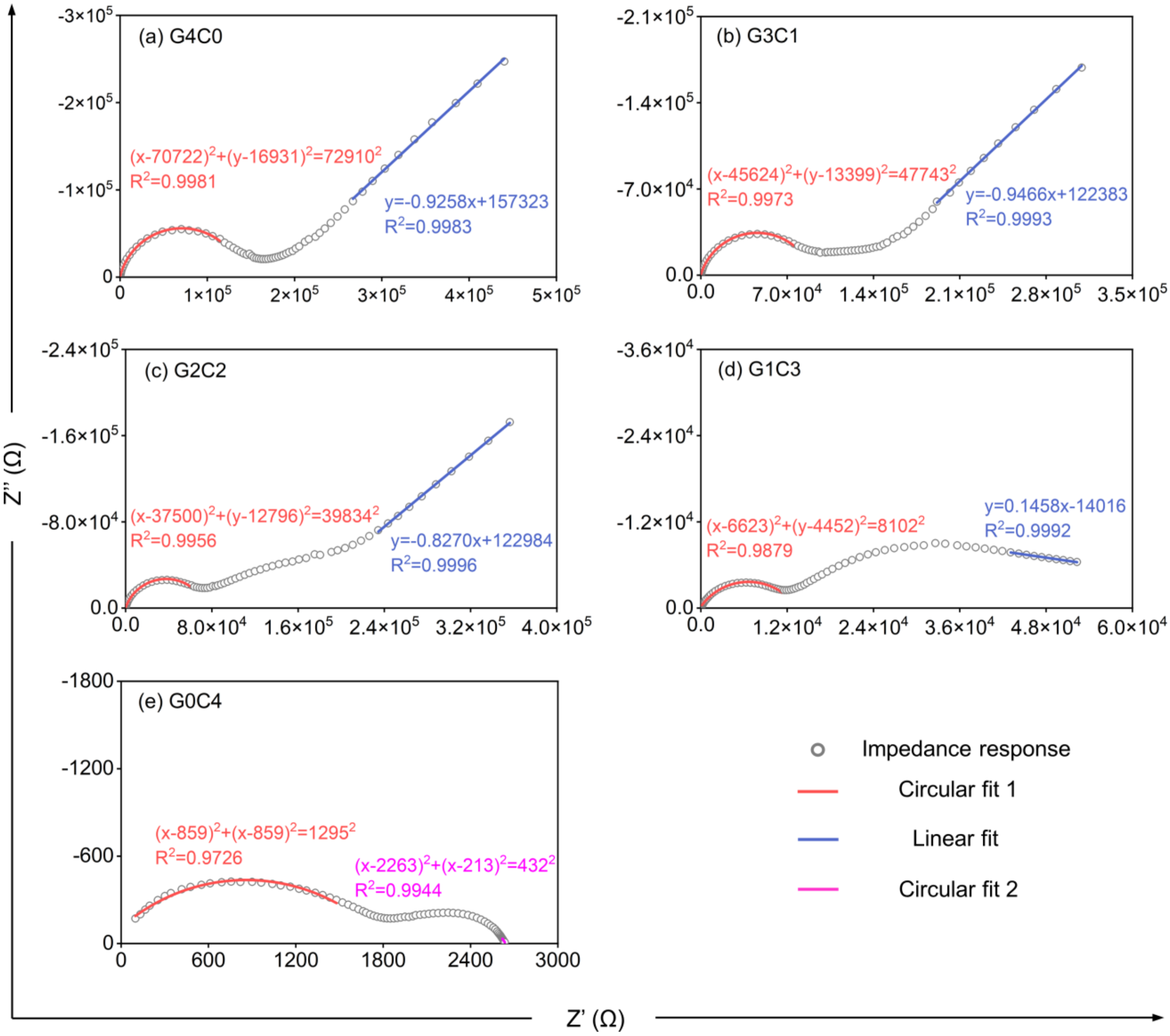

Fig. 11. Complex plane plot and fitting results for the ACIS measurement.

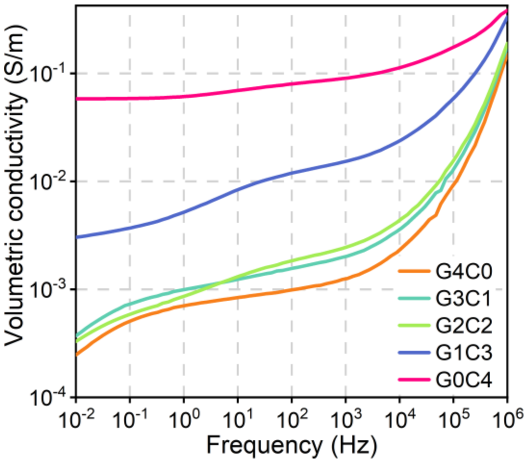

Fig. 12. Volumetric conductivity of G/C-UHPC with various ratios of G/CNT.

3.5 Piezoresistive properties

3.5.1 Under monotonic compression

Fig. 13 presents the relationship between FCR and compressive strain for G/C-UHPC under monotonic compression. It can be observed that the volumetric electrical resistance was sensitive to changes in compressive strain of specimen. G/C-UHPC with varying G/CNT ratios exhibited two distinct piezoresistive behaviours. The FCR curves for G4C0 and G3C1 can be divided into two stages: a linear stage and a nonlinear stage. Here, the value of FCR was found to decrease monotonically up to compressive destruction. The GF value, reflecting the strain sensitivity, can be obtained by linearly fitting the data at the linear stage. Results indicate that the GF value of G4C0 and G3C1 were respectively 11 and 20, which are higher than that of commercial metal strain gauges (about 2) [3] and that of self-sensing UHPC recorded on Refs. [18, 22]. At the nonlinear stage, the rise in strain led to a faster decline in FCR, which can be fitted by an exponential function. The value of R^2 was close to one, suggesting a perfect fit. This feature of the monotonic piezoresistive behaviour is consistent with that presented in Refs. [17, 24]. In contrast, the electrical resistance value of G2C2, G1C3, and G0C4 went through successively three stages including linear decrease (I), balance (II), and abrupt increase (III), which are analogous to the typical piezoresistive behaviour of self-sensing OCC [4]. These stages correspond to compaction, germination and extension of fresh cracks under compression, respectively [4]. The GF values for G2C2, G1C3, and G0C4 were 14, 27, and 28, respectively.

Compared to G4C0, the GF value increased by 81.8%, 27.3%, 145.5%, and 154.5% from G3C1 to G0C4. In addition, as G/CNT ratio dropped, the balance stage tended to appear at the smaller compressive strain for G2C2, G1C3, and G0C4 (from 2.21×10^{-3} to 1.32×10^{-3} to 1.12×10^{-3}).

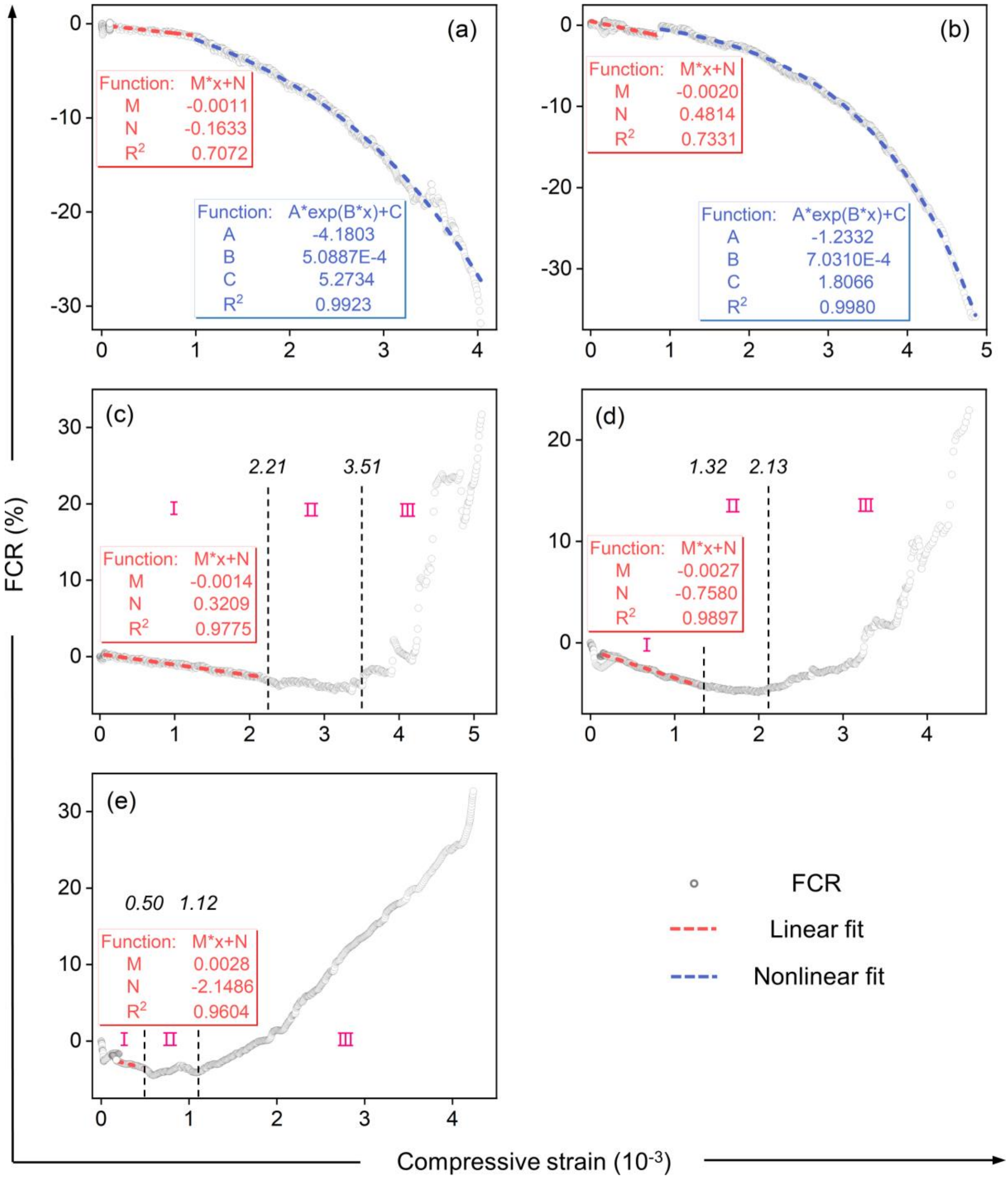

Fig. 13. FCR-compressive strain curve for G/C-UHPC: (a) G4C0, (b) G3C1, (c) G2C2, (d) G1C3, and (e) G0C4.

3.5.2 Under cyclic compression

Fig. 14 shows the time-dependent strain and FCR of G/C-UHPC under cyclic compression. The minimum FCR from G4C0 to G0C4 was found to be -3.59%, -5.11%, -6.40%, -9.21%, and -2.38%, respectively. The FCR signals of G3C1 and G2C2 exhibited better stability and reversibility than those of G4C0. G4C0 was unable to maintain nearly the same electrical resistance as the original state after being subjected to a stress amplitude higher than 1/3 of the compressive strength, while the change trends of FCR and compressive strain for G3C1 and G2C2 had very high goodness-of-fit. The cyclic piezoresistive behaviour of G1C3 and G0C4 showed poor stability and reversibility in this test condition and up to 22.94 and 9.55 values of the FCR monocyclic difference were found. Besides, in contrast to G4C0, the signal fluctuations decreased with decreasing G/CNT ratio, which can be ascribed to the gradually improved conductive network inside G/C-UHPC [18, 26, 29].

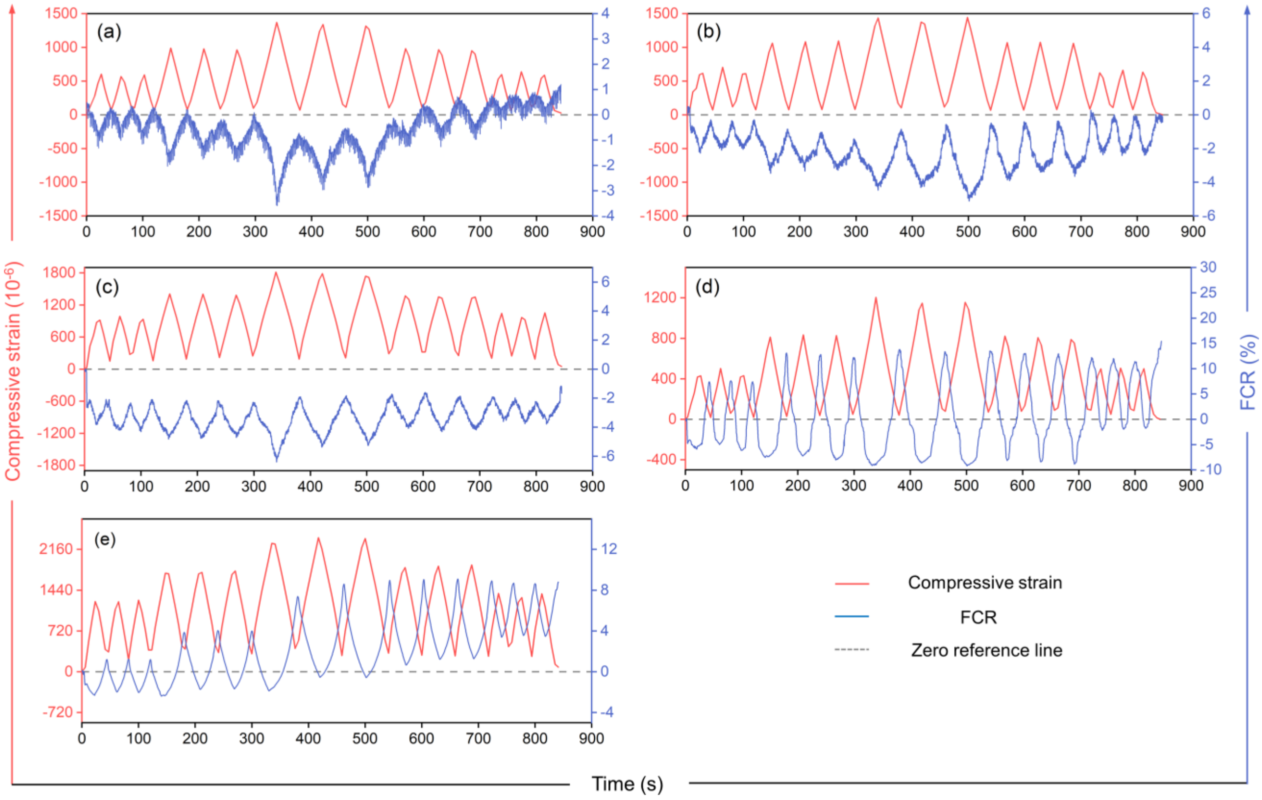

Fig. 14. Cyclic compressive strain- and FCR- time curve for G/C-UHPC: (a) G4C0, (b) G3C1, (c) G2C2, (d) G1C3, and (e) G0C4.

4 Discussion

4.1 Effect of electrical percolation on the piezoresistive behaviour

Piezoresistivity is an electromechanical effect characterized by variations in electrical conductivity in response to compressive strain. Usually, researchers attempt to elucidate their observed piezoresistive behaviour by means of conductive network affected by the deformation and cracking process before and after loading [3-5, 9, 10]. Herein, the continuous conductive network can be formed inside G/C-UHPC matrix by the incorporation of hybrid carbon nanomaterials and steel fibre. Based on the results of compressive, electrical, and piezoresistive tests, it is reasonable to give the conceptual illustration (Fig. 15a) to explain the effect of electrical percolation on piezoresistive behaviour

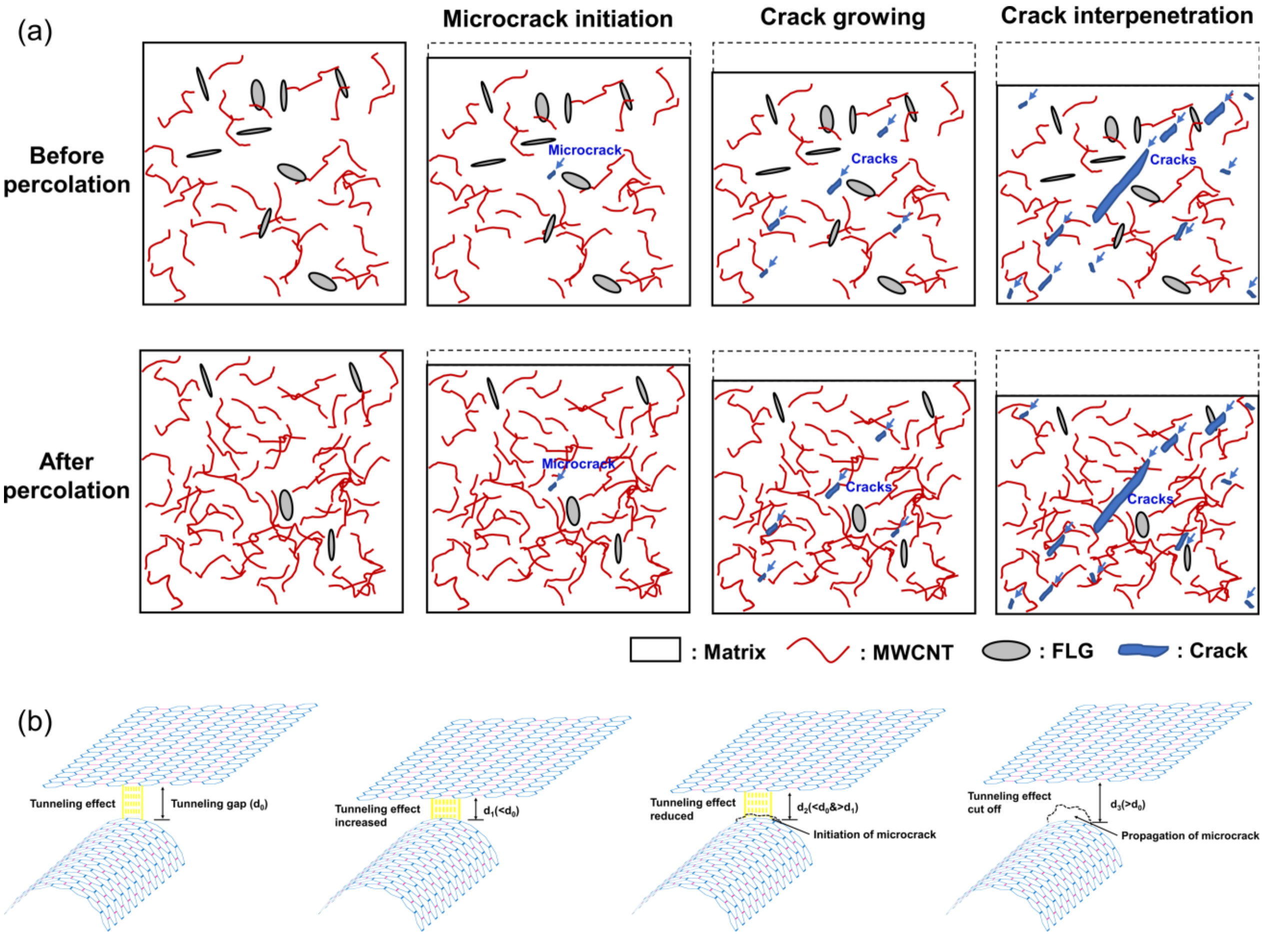

Fig. 15. (a) Effect of deformation and cracking on the conductive pathways before and after electrical percolation and (b) electrical tunnelling effect between conductive nanomaterials affected by elastic deformation and crack evolution for G/C-UHPC.

During the elastic deformation process, there is no damage evolution to the conductive network, along with only a decrease in conductive fillers-matrix interfacial resistance and an improvement in contacting and tunnelling conduction between conductive additives (Fig. 15b), which are caused by the partial close of the micro-voids and the conductive fillers-matrix interfacial gaps [26, 42]. As seen in Fig. 13, from G4C0 to G0C4, FCR is proportional to the compressive strain, namely the linear topological structures of FCR curves do not change for the improvement of conductive network, indicating that the linear decrease of interfacial resistance is dominant in this stage instead of the exponential decline in tunnelling resistance [55]. Moreover, the strain sensitivity (i.e., GF) increased from 11 to 28, which can be attributed to the increment of the conductive mechanism involved interspaces [29], illustrating the positive effect of the improved conductive network on reversible piezoresistive sensitivity.

As the compressive stress continues to go up, the initiation, growth, and interpenetration of microcracks at the area of stress concentration begin to reconstruct the conductive network and become another prominent influence factor to the piezoresistive behaviour in addition to compaction. Taking the electrical tunnelling effect as an instance, as the interfacial gap enlarges, the effect between conductive additives can be weakened and even cut off (Fig. 15b), eventually leading to a considerable rise in volumetric electrical resistance, and meanwhile, the effect elsewhere within G/C-UHPC may be strengthened by compaction [54]. For G4C0 and G3C1 (i.e., before electrical percolation), their electrical resistivity reduced exponentially as the number of matrix cracks went up (Fig. 13). As seen in Fig. 15a, this “atypical” trend compared to G1C3 and G0C4 can be ascribed to two reasons [4]: (1) In the absence of a consecutive conductive network, the non-percolated matrix provides significant space for enhancement in contacting and tunnelling conduction due to high-level strain and the exponential growth of tunnelling conduction is a cause for the nonlinear characteristic [54]. (2) The same cracking process has different reconstruction capabilities for conductive networks with distinct continuity properties, that is, the more inconsecutive the conductive network, the less destructive the cracking. The previous studies [24] explored the reorganization of discontinuous conductive network by cracks from a more macroscopic perspective and reported that the piezoresistive behaviour of self-sensing UHPC with similar characteristic can be attributed to a result of conductive steel fibre bridging at the cracked sections. For G2C2, G1C3, and G0C4, the two competing factors strengthen or weaken with strain under cases of changing continuity of the conductive network, promoting the formation of the balance stage in the FCR-strain curve (Fig. 13). The advance of the balance stage with the decline of G/CNT ratio can be therefore explained by that the potential for contacting and tunnelling conduction improvements is limited and the more consecutive conductive networks are more severely damaged by cracks, as shown in Fig. 15a.

Although it is clear that the type of piezoresistive behaviour for G/C-UHPC depends on the continuity of the conductive network, another point to be noted here is that based on the electrical and piezoresistive results, the piezoresistive behaviour of G2C2 exhibits a typical three-stage pattern without the occurrence of electrical percolation. The functional fillers content of this non-percolated specimen is close to the electrical percolation threshold, generating a consecutive conductive channel during the action of the external load.

4.2 Effect of matrix type on the piezoresistive behaviour

Table 9 presents a summary of the piezoresistive properties of self-sensing cementitious materials collected from literature. It should be mentioned that the inclusion of the contacting resistance due to the two-electrode method and irreversible change in electrical resistance for GF values may be two pitfalls to characterize the piezoresistivity according to Chung [9, 38]. Therefore, attention is paid to the results of the four-electrode method and the inherent GF. The GF value decreased by approximately one to two orders of magnitude from OCC to UHPC. From the standpoint of w/b ratio, identical conclusions can be obtained in Ref. [56] that the application of a higher w/b ratio is relatively more effective to strengthening piezoresistive properties than a lower one. Compared to OCC, UHPC has highly dense microstructures leading to the limited mobility of conductive additives [11, 12, 42], low porosity (Fig. 10) and high elastic modulus. Thus, during the elastic deformation process, the reduction of conductive fillers-matrix interfacial resistance and improvement of contacting and tunnelling conduction between conductive additives in UHPC matrix are weaker than those of OCC.

Moreover, UHPC exhibits a quite linear compressive stress-strain behaviour up to 70%-95% of the amplitude of compressive stress (Fig. 6a), whereas OCC usually shows a linear limit to 1/3 [42]. Such discrepancy means that in the case of UHPC, the formation of penetrating cracks is delayed compared to OCC [22]. Concurrently, UHPC has an elevated toughness due to the presence of multiscale fillers with pinning effect and crack-bridging effect and its ultimate compressive strain (about 4×10^{-3}) is almost twice that of OCC (approximately 2×10^{-3}) [11, 12, 42]. In literature [4], the typical three-stage pattern of piezoresistive behaviour has been confirmed in numerous experimental studies on self-sensing OCC while the aforementioned two-stage pattern is rarely reported, which can be attributed to the destruction of conductive network in advance by penetrating cracks and the limited enhancement of tunnelling conduction due to low compressive strain.

The experimental study indicated that hybrid carbon nanomaterials can be considered as a promising functional additive option for the fabrication of low-porosity, ultra-high-strength, and electrically percolated UHPC-based sensors. However, as one of the most important properties of the self-sensing UHPC, the piezoresistive sensitivity here is still not comparable to that of ordinary cement-based sensors, although it is higher than that reported for many other self-sensing UHPCs. For a wide range of practical applications, it is crucial to explore the manufacturing methods for more sensitive and low-cost self-sensing UHPCs and to create application scenarios that maximize their functionality. For example, use multi-phase, multi-scale, and multi-dimension functional fillers to build hybrid systems as well as use sustainable alternative to conductive fillers such as recycled carbon fibre, rubber waste, recycled ceramics, or biochar. This is the subject of ongoing work and will be presented in a future publication.

Table 9 Summary of existing studies on the piezoresistive properties of various self-sensing cementitious materials.

Matrix	Additives [a]	Concentration [b]	W/b ratio	Compressive strength (MPa)	Measuring type	Electrode configuration	Electrical factors			Ref.
							ρ_0 (Ω·m) [c]	GF type [d]	GF value	
UHPC	SF + G + CNT	2 vol.% (SF) + 0.5 wt.% (G)	0.24	194.7	DC	Four	1.1×10^4	Inherent	11.0	This study
		2 vol.% (SF) + 0.375 wt.% (G) + 0.125 wt.% (CNT)		180.8			6.5×10^3		20.0	
		2 vol.% (SF) + 0.25 wt.% (G) + 0.25 wt.% (CNT)		180.0			3.0×10^3		14.0	
		2 vol.% (SF) + 0.125 wt.% (G) + 0.375 wt.% (CNT)		167.4			1.3×10^3		27.0	
		2 vol.% (SF) + 0.5 wt.% (CNT)		166.3			90.9		28.0	
UHPC	SF	0 vol.%	0.19	80.3	DC	Four	7.6×10^5	Inherent	-	[18]
		0.5 vol.%		91.3			6.1×10^5		7.0	
		1 vol.%		105.3			4.9×10^5		3.7	
		1.5 vol.%		125.7			3.7×10^5		4.6	
		2 vol.%		129.3			3.2×10^5		3.4	
UHPC	SS + G	25 wt.% (SS)	0.20	~124.0	DC	Two	$\sim1.9\times10^4$	-	-	[25]
		25 wt.% (SS) + 0.01 wt.% (G)		127.9			$\sim1.8\times10^4$			
		25 wt.% (SS) + 0.05 wt.% (G)		142.5			6.3×10^3			
		25 wt.% (SS) + 0.1 wt.% (G)		~120.0			$\sim1.0\times10^4$			
UHPC	SF + CNT	2 vol.% (SF) + 0.5 vol.% (CNT)	0.20	164.9	AC (100 kHz)	Four	-	Inherent	9.6	[22]
UHPC	SF + CNT	2 vol.% (SF) + 1.24 wt.% (CNT)	0.19	191.0	DC	Four	-	Irreversible	3610.7	[21]
Mortar	CNT + G	0.5 wt.% (CNT) + 0.5 wt.% (G)	0.44	-	DC	Four	63.6	Inherent	123.9	[57]
		0.85 wt.% (CNT) + 0.85 wt.% (G)	0.52				29.9		139.6	
		1.2 wt.% (CNT) + 1.2 wt.% (G)	0.56				10.6		151.2	
		1.7 wt.% (CNT) + 1.7 wt.% (G)	0.64				8.2		173.5	
Mortar	CNT + G	0.85 wt.% (CNT) + 0.85 wt.% (G)	0.52	-	DC	Four	32.0	Inherent	~45.0	[32]
Paste	CNT + G	1 wt.% (CNT) + 5 wt.% (G)	0.40	-	DC	Four	0.4	Inherent	17.4	[58]

[a] SF and SS are the abbreviations of steel fibre and steel slag, respectively.

[b] wt.% and vol.% refer to the conductive additives by the weight of binders and by the volume of matrix, respectively.

[c] $\rho_0=R_0S/L$, where S is the contacting surface between the electrode and specimen and L is the spacing between the two inner electrodes.

[d] The inherent GF value is obtained from the reversible change in electrical resistivity due to elastic deformation. Contrarily, the irreversible GF value consists of the irreversible change because of damage and plastic deformation [9].

5 Conclusions

This study experimentally investigated the piezoresistive behaviour and mechanisms of self-sensing ultra-high performance concrete (UHPC) containing 0.5 wt.% of hybrid graphene (G) and carbon nanotube (CNT) with various mass ratios, i.e., 4:0 (G4C0), 3:1 (G3C1), 2:2 (G2C2), 1:3 (G1C3), and 0:4 (G0C4). A series of tests were conducted to explore the workability, mechanical properties, electrical properties, and microstructural characteristics of G/C-UHPC. From the experimental results, the main conclusions can be drawn as follows:

(1) As the ratio of G/CNT drops from 4:0 to 0:4, the macroscopic deformation and cracking process of G/C-UHPC tend to be similar and the uniaxial compressive strength reduces from 194.7 MPa to 166.3 MPa as a result of the strong water absorption and aggregation effect due to the increased specific surface area of carbon nanomaterials.

(2) G sufficiently disperses in UHPC matrix. CNT forms bridges between adjacent G lamella, establishing a filler distribution network that improved the external stress-bearing capacity. With the increase of CNT proportion, the volume of small and medium capillary pores declines and that of large capillary pores and air holes increases. Compared to G4C0, the porosity of G3C1, G2C2, G1C3, and G0C4 reduces by 25.1%, 35.0%, 42.8%, and 26.8%, respectively, implying the pore refinement.

(3) With the increase of the proportion of CNT, the impedance response of G/C-UHPC shifts to the left and the radius value of arc declines from 72910 Ω to 1295 Ω. Electrical percolation takes place at G1C3 and G0C4.

(4) Regarding the piezoresistive behaviour under monotonic compression, the fractional change of resistance (FCR) curves for G4C0 and G3C1 can be divided into a linear stage and a nonlinear stage with gauge factor (GF) values of 11 and 20, respectively. As CNT fraction increases, the FCR curves for G2C2, G1C3, and G0C4 undergo three stages, including linear decrease, balance, and abrupt increase, with GF values of 14, 27, and 28,

respectively. Under cyclic compression, the electrical signal fluctuation declines with increasing CNT content. FCR signals of G3C1 and G2C2 exhibit better stability and reversibility compared to the other three groups.

(5) Differential reorganizational responses of conductive network with different continuity (i.e., electrical percolation or not) to elastic deformation as well as initiation, growth, and interpenetration of cracks under monotonic compression can be the underlying reason why the self-sensing UHPCs with different ratios of G/CNT produce different shapes of the FCR versus compressive strain curves.

CRediT authorship contribution statement

Facheng Song: Conceptualization, Methodology, Investigation, Formal analysis, Writing-Original Draft, Writing-Review & Editing. **Qing Chen:** Conceptualization, Supervision, Funding Acquisition, Writing-Review & Editing. **Mingzhong Zhang:** Writing-Review & Editing. **Zhengwu Jiang:** Resources, Supervision, Funding Acquisition. **Wenqi Ding:** Writing-Review & Editing. **Zhiguo Yan:** Writing-Review & Editing. **Hehua Zhu:** Supervision, Funding Acquisition.

Declaration of Competing Interest

The authors declare that they have no known competing financial interests or personal relationships that could have appeared to influence the work reported in this paper.

Acknowledgments

The authors gratefully acknowledge the financial supports provided by National Key Research and Development Projects (2022YFC3803104) and National Natural Science Foundation of China (52122808, 52078381, 51878496). The authors also thank Shiyanjia Lab (www.shiyanjia.com) for the MIP analysis.

References

[1] Z.Z. Deng, W.G. Li, W.K. Dong, Z.H. Sun, J. Kodikara, D.C. Sheng, Multifunctional asphalt concrete pavement toward smart transport infrastructure: Design, performance and perspective, Compos. Pt. B-Eng. 265 (2023) 110937. https://doi.org/10.1016/j.compositesb.2023.110937.

[2] F.C. Song, Q. Chen, Q.M. Zheng, Multifunctional ultra-high performance fibre-reinforced concrete with integrated self-sensing and repair capabilities towards in-situ structure monitoring, Compos. Struct. 321 (2023) 117240. https://doi.org/10.1016/j.compstruct.2023.117240.

[3] D.D.L. Chung, A critical review of electrical-resistance-based self-sensing in conductive cement-based materials, Carbon, 203 (2023) 311-325. https://doi.org/10.1016/j.carbon.2022.11.076.

[4] B.G. Han, S.Q. Ding, X. Yu, Intrinsic self-sensing concrete and structures: A review, Measurement, 59 (2015) 110-128. https://doi.org/10.1016/j.measurement.2014.09.048.

[5] X.R. Wang, Q.H. Li, H.X. Lai, Y. Peng, S.L. Xu, Broadband microwave absorption enabled by a novel carbon nanotube gratings/cement composite metastructure, Compos. Pt. B-Eng. 242 (2022) 110071. https://doi.org/10.1016/j.compositesb.2022.110071.

[6] A. Al-Dahawi, G. Yildirim, O. Ozturk, M. Sahmaran, Assessment of self-sensing capability of Engineered Cementitious Composites within the elastic and plastic ranges of cyclic flexural loading, Constr. Build. Mater. 145 (2017) 1-10. https://doi.org/10.1016/j.conbuildmat.2017.03.236.

[7] G. Yildirim, O. Ozturk, A. Al-Dahawi, A.A. Ulu, M. Sahmaran, Self-sensing capability of Engineered Cementitious Composites: Effects of aging and loading conditions, Constr. Build. Mater. 231 (2020) 117132. https://doi.org/10.1016/j.conbuildmat.2019.117132.

[8] G. Yildirim, M.H. Sarwary, A. Al-Dahawi, O. Ozturk, O. Anil, M. Sahmaran, Piezoresistive behavior of CF- and CNT-based reinforced concrete beams subjected to static flexural loading: Shear failure investigation, Constr. Build. Mater. 168 (2018) 266-279. https://doi.org/10.1016/j.conbuildmat.2018.02.124.

[9] D.D.L. Chung, A critical review of piezoresistivity and its application in electrical-resistance-based strain sensing, J. Mater. Sci. 55 (32) (2020) 15367-15396. https://doi.org/10.1007/s10853-020-05099-z.

[10] W.G. Li, W.K. Dong, Y.P. Guo, K.J. Wang, S.P. Shah, Advances in multifunctional cementitious composites with conductive carbon nanomaterials for smart infrastructure, Cem. Concr. Compos. 128 (2022) 104454. https://doi.org/10.1016/j.cemconcomp.2022.104454.

[11] J.H. Gong, Y.W. Ma, J.Y. Fu, J. Hu, X.W. Ouyang, Z.H. Zhang, H. Wang, Utilization of fibers in ultra-high performance concrete: A review, Compos. Pt. B-Eng. 241 (2022) 109995. https://doi.org/10.1016/j.compositesb.2022.109995.

[12] H.W. Zhang, Z.M. Wu, X. Hu, X. Ouyang, Z.H. Zhang, N. Banthia, C.J. Shi, Design, production, and properties of high-strength high-ductility cementitious composite (HSHDCC): A review, Compos. Pt. B-Eng. 247 (2022) 110258. https://doi.org/10.1016/j.compositesb.2022.110258.

[13] Y. Bae, S. Pyo, Ultra high performance concrete (UHPC) sleeper: Structural design and performance, Eng. Struct. 210 (2020) 110374. https://doi.org/10.1016/j.engstruct.2020.110374.

[14] Y. Bae, S. Pyo, Effect of steel fiber content on structural and electrical properties of ultra high performance concrete (UHPC) sleepers, 222 (2020) 111131. https://doi.org/10.1016/j.engstruct.2020.111131.

[15] M.Q. Sun, R.J.Y. Liew, M.H. Zhang, W. Li, Development of cement-based strain sensor for health monitoring of ultra high strength concrete, Constr. Build. Mater. 65 (2014) 630-637. https://doi.org/10.1016/j.conbuildmat.2014.04.105.

[16] J.K. Lian, C. Hu, T.F. Fu, Y.L. Wang, Review of self-sensing capability of ultra-high performance concrete, Front. Mater. 8 (2021) 746022. https://doi.org/10.3389/fmats.2021.746022.

[17] S.F. Dong, B.G. Han, J.P. Ou, Z. Li, L.Y. Han, X. Yu, Electrically conductive behaviours and mechanisms of short-cut super-fine stainless wire reinforced reactive powder concrete, Cem. Concr. Compos. 72 (2016) 48-65. https://doi.org/10.1016/j.cemconcomp.2016.05.022.

[18] Y.Y. Hou, M.Q. Sun, J.Z. Chen, Electrical resistance and capacitance responses of smart ultra-high performance concrete with compressive strain by DC and AC measurements, Constr. Build. Mater. 327 (2022) 127007. https://doi.org/10.1016/j.conbuildmat.2022.127007.

[19] M.K. Kim, D.J. Kim, Y.K. An, Electro-mechanical self-sensing response of ultra-high-performance fiber-reinforced concrete in tension, Compos. Pt. B-Eng. 134 (2018) 254-264. https://doi.org/10.1016/j.compositesb.2017.09.061.

[20] H. Wang, F.T. Shi, J.L. Shen, A.L. Zhang, L.C. Zhang, H.H. Huang, J.Z. Liu, K.K. Jin, L.Y. Feng, Z.Y. Tang, Research on the self-sensing and mechanical properties of aligned stainless steel fibre-reinforced reactive powder concrete, Cem. Concr. Compos. 119 (2021) 104001. https://doi.org/10.1016/j.cemconcomp.2021.104001.

[21] M. Jung, J. Park, S.G. Hong, J. Moon, Electrically cured ultra-high performance concrete (UHPC) embedded with carbon nanotubes for field casting and crack sensing, Mater. Des. 196 (2020) 109127. https://doi.org/10.1016/j.matdes.2020.109127.

[22] S.H. Lee, S. Kim, D.Y. Yoo, Hybrid effects of steel fibre and carbon nanotube on self-sensing capability of ultra-high-performance concrete, Constr. Build. Mater. 185 (2018) 530-544. https://doi.org/10.1016/j.conbuildmat.2018.07.071.

[23] J. Seo, D. Jang, B.M. Yang, H.N. Yoon, J.G. Jang, S. Park, H. Lee, Material characterization and piezoresistive sensing capability assessment of thin-walled CNT-embedded ultra-high performance concrete, Cem. Concr. Compos. 134 (2022) 104808. https://doi.org/10.1016/j.cemconcomp.2022.104808.

[24] I. You, D.Y. Yoo, S. Kim, M.J. Kim, G. Zi, Electrical and self-sensing properties of ultra-high-performance fibre-reinforced concrete with carbon nanotubes, Sensors, 17 (11) (2017) 2481. https://doi.org/10.3390/s17112481.

[25] L.P. Guo, J.D. Wu, H. Wang, Mechanical and perceptual characterization of ultra-high-performance cement-based composites with silane-treated graphene nano-platelets, Constr. Build. Mater. 240 (2020) 117926. https://doi.org/10.1016/j.conbuildmat.2019.117926.

[26] F.C. Song, Q. Chen, Z.W. Jiang, X.P. Zhu, B. Li, B. He, H.H. Zhu, Piezoresistive properties of ultra-high-performance fibre-reinforced concrete incorporating few-layer graphene, Constr. Build. Mater. 305 (2021) 124362. https://doi.org/10.1016/j.conbuildmat.2021.124362.

[27] H.V. Le, M.K. Kim, D.J. Kim, J. Park, Electrical properties of smart ultra-high performance concrete under various temperatures, humidities, and age of concrete, Cem. Concr. Compos. 118 (2021) 103979. https://doi.org/10.1016/j.cemconcomp.2021.103979.

[28] H.V. Le, M.K. Kim, S.U. Kim, S.Y. Chung, D.J. Kim, Enhancing self-stress sensing ability of smart ultra-high performance concretes under compression by using nano functional fillers, J. Build. Eng. 44 (2021) 102717. https://doi.org/10.1016/j.jobe.2021.102717.

[29] A. Hussain, Y. Xiang, T. Yu, F.X. Zou, Nanocarbon black-based ultra-high-performance concrete (UHPC) with self-strain sensing capability, Constr. Build. Mater. 359 (2022) 129496. https://doi.org/10.1016/j.conbuildmat.2022.129496.

[30] B. Joshi, J.J. Wang, X.L. Li, N.H. Ramaswamy, P. Shrestha, X.N. Shan, Y.L. Mo, T.T.C. Hsu, Development of robust ultra-high-performance carbon nanofiber aggregates (UHPCNFAs) for structural health monitoring, Eng. Struct. 279 (2023) 115559. https://doi.org/10.1016/j.engstruct.2022.115559.

[31] X.Y. Wang, B.Y. Cao, C. Vlachakis, A. Al-Tabbaa, S.K. Haigh, Characterization and piezo-resistivity studies on graphite-enabled self-sensing cementitious composites with high stress and strain sensitivity, Cem. Concr. Compos. 142 (2023) 105187. https://doi.org/10.1016/j.cemconcomp.2023.105187.

[32] M. Abedi, R. Fangueiro, A.G. Correia, Effects of multiscale carbon-based conductive fillers on the performances of a self-sensing cementitious geocomposite, J. Build. Eng. 43 (2021) 103171. https://doi.org/10.1016/j.jobe.2021.103171.

[33] M. Abedi, R. Fangueiro, A. Camoes, A.G. Correia, Evaluation of CNT/GNP's synergic effects on the Mechanical, Microstructural, and durability properties of a cementitious composite by the novel dispersion method, Constr. Build. Mater. 260 (2020) 120486. https://doi.org/10.1016/j.conbuildmat.2020.120486.

[34] G. Hong, S. Choi, D.Y. Yoo, T. Oh, Y. Song, J.H. Yeon, Moisture dependence of electrical resistivity in under-percolated cement-based composites with multi-walled carbon nanotubes, J. Mater. Res. Technol-JMRT, 16 (2022) 47-58. https://doi.org/10.1016/j.jmrt.2021.11.151.

[35] B. Zou, S.J. Chen, A.H. Korayem, F. Collins, C.M. Wang, W.H. Duan, Effect of ultrasonication energy on engineering properties of carbon nanotube reinforced cement pastes, Carbon, 85 (2015) 212-220. https://doi.org/10.1016/j.carbon.2014.12.094.

[36] X.P. Zhu, C. Qian, B. He, Q. Chen, Z.W. Jiang, Experimental study on the stability of C-S-H nanostructures with varying bulk CaO/SiO2 ratios under cryogenic attack, Cem. Concr. Res. 135 (2020) 106114. https://doi.org/10.1016/j.cemconres.2020.106114.

[37] X.P. Zhu, Q. Ren, B. He, H.E. Zhang, Z.W. Zhang, Upscaling degradation of cementitious calcium (aluminate) silicate hydrate upon ultra-low temperature attack: A multiscale insight and a bottom-up enhancement route, Compos. Pt. B-Eng. 243 (2022) 110122. https://doi.org/10.1016/j.compositesb.2022.110122.

[38] D.D.L. Chung, Pitfalls in piezoresistivity testing, J. Electron. Mater. 51 (10) (2022) 5473-5481. https://doi.org/10.1007/s11664-022-09857-4.

[39] L.M. Liu, Z. Fang, Z.Y. Huang, Y.Y. Wu, Solving shrinkage problem of ultra-high-performance concrete by a combined use of expansive agent, super absorbent polymer, and shrinkage-reducing agent, Compos. Pt. B-Eng. 230 (2022) 109503. https://doi.org/10.1016/j.compositesb.2021.109503.

[40] D. Feys, R. Verhoeven, G. De Schutter, Why is fresh self-compacting concrete shear thickening? Cem. Concr. Res. 39 (6) (2009) 510-523. https://doi.org/10.1016/j.cemconres.2009.03.004.

[41] A. Arora, M. Aguayo, H. Hansen, C. Castro, E. Federspiel, B. Mobasher, N. Neithalath, Microstructural packing- and rheology-based binder selection and characterization for Ultra-high Performance Concrete (UHPC), Cem. Concr. Res. 103 (2018) 179-190. https://doi.org/10.1016/j.cemconres.2017.10.013.

[42] X. Ouyang, Z.M. Wu, B. Shan, Q. Chen, C.J. Shi, A critical review on compressive behaviour and empirical constitutive models of concrete, Constr. Build. Mater. 323 (2022) 126572. https://doi.org/10.1016/j.conbuildmat.2022.126572.

[43] ACI Committee 239, Ultra-high Performance Concrete, ACI Fall Convention., Toronto, Ontario, Canada, 2012.

[44] Y.H. Du, J. Yang, B.S. Thomas, L.H. Li, H.Y. Li, S. Nazar, Hybrid graphene oxide/carbon nanotubes reinforced cement paste: An investigation on hybrid ratio, Constr. Build. Mater. 261 (2020) 119815. https://doi.org/10.1016/j.conbuildmat.2020.119815.

[45] X.P. Zhu, L. Brochard, M. Vandamme, Z.W. Jiang, Scaling of nanoscale elastic and tensile failure properties of cementitious calcium-silicate-hydrate materials at cryogenic temperatures: A molecular simulation study, Cem. Concr. Res. 172 (2023) 107242. https://doi.org/10.1016/j.cemconres.2023.107242.

[46] X.P. Zhu, Q. Ren, B. He, H.E. Zhang, Z.W. Jiang, The nanomechanical nature of cementitious calcium-(alumino) silicate-hydrate under ultra-low temperature attack: An intrinsic transition and the role of aluminum for bottom-up enhancement, Cem. Concr. Compos. 134 (2022) 104811. https://doi.org/10.1016/j.cemconcomp.2022.104811.

[47] X.P. Zhu, M. Vandamme, L. Brochard, Z.L. Zhang, Q. Ren, C. Li, B. He, H.E. Zhang, Y. Zhang, Q. Chen, Z.W. Jiang, Nature of aluminates in C-A-S-H: A cryogenic stability insight, an extension of DNA-code rule, and a general structural-chemical formula, Cem. Concr. Res. 167 (2023) 107131. https://doi.org/10.1016/j.cemconres.2023.107131.

[48] K.L. Scrivener, R. Snellings, B. Lothenbach, A practical guide to microstructural analysis of cementitious materials, CRC Press, Taylor & Francis Group, 2016. https://doi.org/10.1201/b19074.

[49] T. Meng, K.J. Ying, H.Y. Yu, Y.P. Hong, An approach to effectively improve the interfacial bonding of paste–limestone by incorporating different nanomaterials, Compos. Pt. B-Eng. 242 (2022) 110046. https://doi.org/10.1016/j.compositesb.2022.110046.

[50] L. Liu, X.C. Wang, J. Zhou, H.Q. Chu, D.J. Shen, H.S. Chen, S.N. Qin, Investigation of pore structure and mechanical property of cement paste subjected to the coupled action of freezing/thawing and calcium leaching, Cem. Concr. Res. 109 (2018) 133-146. https://doi.org/10.1016/j.cemconres.2018.04.015.

[51] J.H. Liu, M.S. Wang, N.N. Liu, L. Teng, Y.F. Wang, Z. Chen, C.J. Shi, Development of ultra-fine SAP powder for lower-shrinkage and higher-strength cement pastes made with ultra-low water-to-binder ratio, Compos. Pt. B-Eng. 262 (2023) 110810. https://doi.org/10.1016/j.compositesb.2023.110810.

[52] H.H. Huang, L. Teng, X.J. Gao, K.H. Khayat, F.Z. Wang, Z.C. Liu, Effect of carbon nanotube and graphite nanoplatelet on composition, structure, and nano-mechanical properties of C-S-H in UHPC, Cem. Concr. Res. 154 (2022) 106713. https://doi.org/10.1016/j.cemconres.2022.106713.

[53] B. Suryanto, W.J. McCarter, G. Starrs, G.V. Ludford-Jones, Electrochemical immittance spectroscopy applied to a hybrid PVA/steel fibre engineered cementitious composite, Mater. Des. 105 (2016) 179-189. https://doi.org/10.1016/j.matdes.2016.05.037.

[54] C.Y. Li, T.W. Chou, Modeling of damage sensing in fibre composites using carbon nanotube networks, Compos. Sci. Technol. 68 (15-16) (2008) 3373-3379. https://doi.org/10.1016/j.compscitech.2008.09.025.

[55] H. Aguilar-Bolados, M. Yazdani-Pedram, A. Contreras-Cid, M.A. Lopez-Manchado, A. May-Pat, F. Aviles, Influence of the morphology of carbon nanostructures on the piezoresistivity of hybrid natural rubber nanocomposites, Compos. Pt. B-Eng. 109 (2017) 147-154. https://doi.org/10.1016/j.compositesb.2016.10.057.

[56] B.G. Han, X. Yu, E. Kwon, J.P. Ou, Effects of CNT concentration level and water/cement ratio on the piezoresistivity of CNT/cement composites, J. Compos. Mater. 46 (1) (2012) 19-25. https://doi.org/10.1177/0021998311401114.

[57] M. Abedi, R. Fangueiro, A.G. Correia, Development of a Novel Multifunctional Cementitious-Based Geocomposite by the Contribution of CNT and GNP, Nanomaterials, 11 (4) (2021) 961. https://doi.org/10.3390/nano11040961.

[58] B. del Moral, F.J. Baeza, R. Navarro, O. Galao, E. Zornoza, J. Vera, C. Farcas, P. Garces, Temperature and humidity influence on the strain sensing performance of hybrid carbon nanotubes and graphite cement composites, Constr. Build. Mater. 284 (2021) 122786. https://doi.org/10.1016/j.conbuildmat.2021.122786.